Chinese Journal of
POLYMER SCIENCE

RESEARCH ARTICLE

https://doi.org/10.1007/s10118-026-3746-y
Chinese J. Polym. Sci.

Robust Intrinsically Stretchable Organic Photodetectors Enabled by High-molecular-weight Conjugated Polymer Fibrils

He-Bing Nie[a], Lu Hao[a], Jing-Chuan Chen[a], Zhi-Yuan Yang[a], Xue-Fei Wu[b*], Zhi-Qin Xia[c], Wan-Cheng Yu[d], Xue-Chen Jiao[d], Wen-Kai Zhong[a*], and Fei Huang[a*]

[a] *Institute of Polymer Optoelectronic Materials and Devices, Guangdong Basic Research Center of Excellence for Energy and Information Polymer Materials, State Key Laboratory of Luminescent Materials and Devices, South China University of Technology, Guangzhou 510640, China*
[b] *Interdisciplinary Research Center for Chemical, Life and Health Sciences, Institute of Chemistry, Chinese Academy of Sciences, Beijing 100190, China*
[c] *Materials Sciences Division, Lawrence Berkeley National Laboratory, Berkeley CA 94720, United States*
[d] *National Synchrotron Radiation Laboratory, University of Science and Technology of China, Hefei 230026, China*

Electronic Supplementary Information

Abstract Intrinsically stretchable organic photodetectors (IS-OPDs) are highly attractive for applications such as skin-mounted wearables, soft robotics, and electronic textiles. However, simultaneously achieving mechanical robustness and stable optoelectronic functionality under high strain remains a challenge. Here, we demonstrate that the fibrillar network morphology formed by high-molecular-weight conjugated polymer blends provides an effective pathway to overcome this limitation. The entangled, interconnected polymer fibrils establish a mechanically percolated network that efficiently dissipates strain energy and suppresses crack propagation, enabling a high fracture strain of about 80% and enhanced toughness. The fibrillar network also forms continuous charge transport pathways, resulting in improved carrier mobility and reduced trap density. Therefore, the IS-OPDs exhibit outstanding performance stability under large deformations, maintaining a high detectivity of about 10^{12} Jones at strains above 40%, while enabling reliable optical communication and clear imaging capability even at 100% strain. Our study identifies a high-molecular-weight-driven fibrillar morphology as a key structural motif for mechanically robust IS-OPDs.

Keywords Conjugated polymers; Fibrillar morphology; Stretchable electronics; Organic photodetectors

Citation: Nie, H. B.; Hao, L.; Chen, J. C.; Yang, Z. Y.; Wu, X. F.; Xia, Z. Q.; Yu, W. C.; Jiao, X. C.; Zhong, W. K.; Huang, F. Robust intrinsically stretchable organic photodetectors enabled by high-molecular-weight conjugated polymer fibrils. *Chinese J. Polym. Sci.* https://doi.org/10.1007/s10118-026-3746-y

INTRODUCTION

Stretchable photodetectors have emerged as next-generation soft optoelectronics with promising applications such as skin-mounted wearable sensors, soft robotics, and electronic textiles.[1–5] In these scenarios, photodetectors must operate reliably under large and repeated mechanical strains (*e.g.*, about 42% for finger joints, about 45% for wrists, about 63% for elbows, and about 100% for knees),[6,7] while maintaining stable photoresponse, low noise, fast response, and high detectivity. Organic semiconductors are attractive for such applications because of their mechanical compliance and solution processability.[8–12] However, achieving intrinsically stretchable organic photodetectors (IS-OPDs) that can simultaneously tolerate large tensile strains and preserve optoelectronic functionality remains a central challenge.[13–15] This difficulty arises from the intrinsic conflict between the structural order required for efficient charge generation and transport and the mechanical compliance needed to accommodate large deformations without fracture or performance degradation.

Current strategies to address this limitation have focused on molecular-level designs or compositional modifications. Typical approaches include synthesizing stretchable conjugated polymers with flexible side chains or backbones,[16–21] incorporating dynamic or noncovalent interactions,[22–26] or blending photoactive materials with elastomeric matrices to improve the mechanical softness.[27–30] While these methods can enhance stretchability, they often compromise charge transport, increase energetic disorder, or dilute the photoactive phase, ultimately limiting photodetection performance.

However, engineering thin-film morphologies beyond the molecular scale is still out of reach.[31–33] In organic semiconductors, both mechanical and electronic properties are governed by hierarchical structures spanning multiple length scales, from chemical structures to molecular packing, and mesoscale phase separation. Deficiencies at any structural level can degrade overall device performance.[34] In this context, fibrillar morphologies have been widely recognized as

* Corresponding authors, E-mail: wuxuefei@iccas.ac.cn (X.F.W.)
E-mail: wkzhong@scut.edu.cn (W.K.Z.)
E-mail: msfhuang@scut.edu.cn (F.H.)
Special Topic: Flexible Polymer Electronics
Received December 21, 2025; Accepted May 14, 2026; Published online August 22, 2026

highly desirable in organic solar cells and organic photodetectors because they promote efficient exciton dissociation and provide continuous percolation pathways for charge transport.[35–40] However, the exploitation of fibrillar architectures to simultaneously address the mechanical robustness and optoelectronic stability of IS-OPDs remains unexplored.

Here, we demonstrate that the fibrillar network morphology formed by high-molecular-weight conjugated polymer blends offers an effective route to resolving this long-standing trade-off (Fig. 1a). We show that kinetically controlled polymer crystallization, enabled by solution processing with *ortho*-dichlorobenzene (*o*-DCB), drives the formation of an interconnected fibrillar network composed of entangled high-molecular-weight polymer chains (Fig. 1b). This mechanically percolated fibrillar network provides efficient strain-energy dissipation pathways, enabling a high fracture strain (>80%) and enhanced toughness (Fig. 1c and Table S1 in the electronic supplementary information, ESI). The fibrillar network also serves as a continuous charge-transport highway, reducing trap states and recombination while facilitating efficient carrier transport and balancing photodetection performance (Fig. 1d). The synergistic combination of mechanical energy dissipation and electronic percolation allows IS-OPDs to maintain stable photodetection performance under large deformations. Our results establish a high-molecular-weight-driven fibrillar network morphology as a powerful multi-scale structural motif for balancing the mechanical durability and optoelectronic functionality in IS-OPDs.

RESULTS AND DISCUSSION

Systems Selection and Multi-scale Morphology

To validate our proposed strategy of leveraging high-molecular-weight-driven fibrillar networks for IS-OPDs, we employed an all-polymer system consisting of PQM-Cl as the donor and P(NDI2OD-T2) as the acceptor. Both polymers incorporated thiophene-based conjugated backbones with pronounced intrachain torsional flexibility, which promoted conformational disorder and facilitated chain entanglement at high molecular weights. The number-average molecular weights are 82.7 kDa for PQM-Cl and 53.3 kDa for P(NDI2OD-T2) as determined by high-temperature gel permeation chromatography (Fig. S1 in ESI). The UV-Vis-NIR absorption spectra of the neat and blended films demonstrate complementary absorption across the visible region (Fig. S2 in ESI), supporting a broadband photoresponse, while providing a suitable platform to explore the morphology-

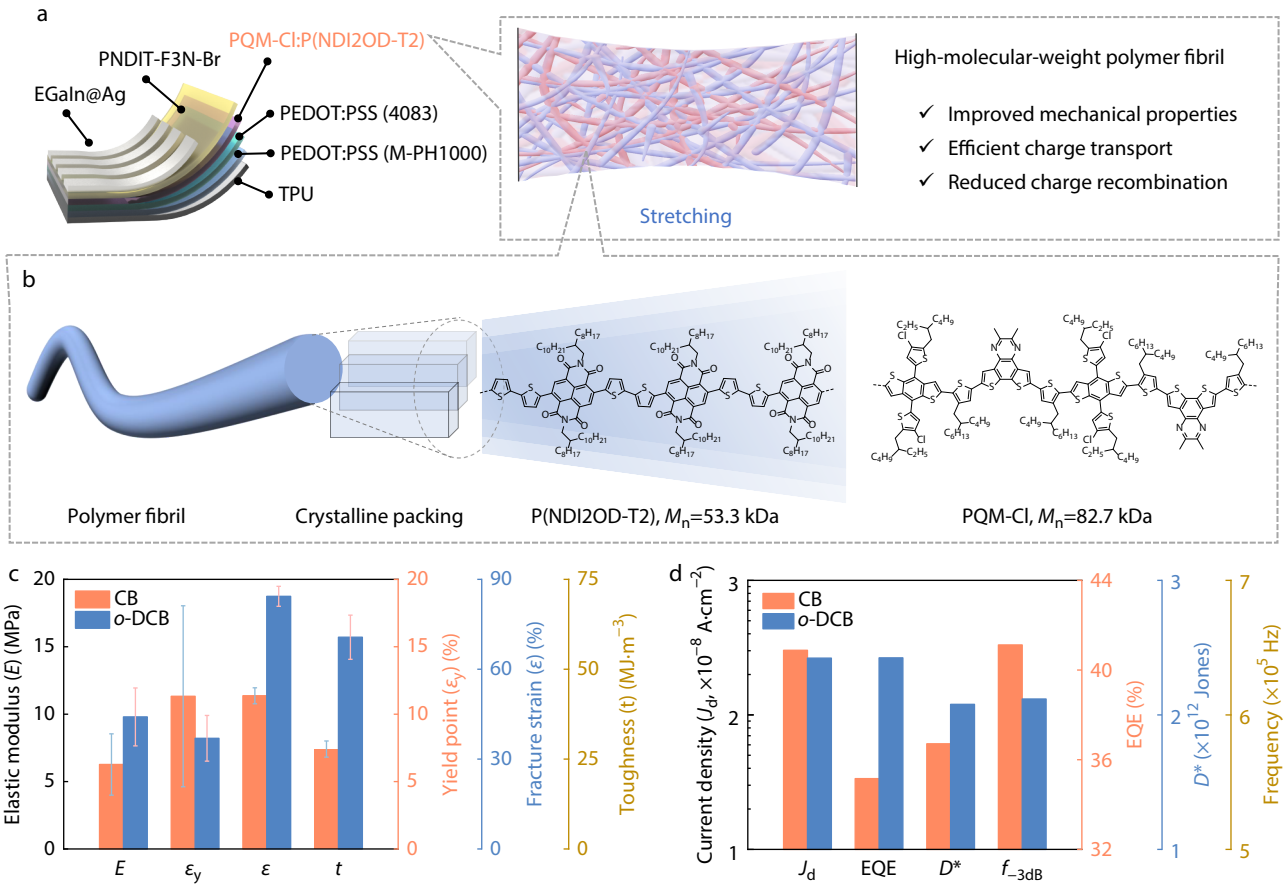

Fig. 1 (a) Schematic illustration of the IS-OPD device architecture, highlighting a photoactive blend film composed of high-molecular-weight conjugated polymers that form an interconnected fibrillar network, enabling enhanced mechanical robustness and efficient charge transport with suppressed trap states; (b) Schematic representation of conjugated polymer fibrils formed through crystallization of PQM-Cl and P(NDI2OD-T2) chains; (c) Comparison of elastic modulus (*E*), yield point (ε_y), fracture strain (ε), and toughness (t) for blend films processed from CB and *o*-DCB; (d) Summary of photodetection performance metrics of OPDs fabricated using CB- and *o*-DCB-processed active layers.

https://doi.org/10.1007/s10118-026-3746-y

property relationships in IS-OPDs.

To regulate crystallization-driven phase separation and thereby access distinct multi-scale morphologies, blend films were processed from chlorobenzene (CB) and *o*-DCB, which differ significantly in their boiling points (132 °C versus 180 °C). *In situ* absorption spectra during solution drying revealed comparable (0-0)/(0-1) vibronic peak ratios for CB and *o*-DCB at the initial stage, indicating similar aggregation states in solution (Fig. 2a and Fig. S3 in ESI). However, *o*-DCB processing extended the film formation timescale from about 2 s (CB) to about 27 s for PQM-Cl, providing a sufficient time window for polymer chain rearrangement and self-assembly (Fig. 2b). This prolonged drying process enables a more complete chain reorganization during film formation, directing distinct crystallization pathways and phase separation behavior.

Grazing incidence wide-angle X-ray scattering (GIWAXS) reveals that both films adopt a predominantly face-on orientation, with pronounced π-π stacking reflection at 1.64 Å^{-1} in the out-of-plane (OOP) direction and lamellar reflection at 0.2–0.4 Å^{-1} in the in-plane (IP) direction, favorable for vertical charge transport in OPDs (Figs. 2c and 2d). Compared with CB processing, the *o*-DCB blend showed significantly enhanced crystallization with better-defined lamellar ordering. Multi-peak fitting revealed increased lamellar coherence lengths of 181 Å for P(NDI2OD-T2) and 58 Å for PQM-Cl, which are substantially higher than those of the CB blend (77 and 55 Å, respectively; Fig. S4 and Table S2 in ESI). The *o*-DCB blend also exhibited enhanced crystallinity, as evidenced by an approximately 18% increase in the total lamellar peak area relative to that of the CB-processed film. Such enhanced crystallization reflects more effective chain rearrangement during slow solvent evaporation, favoring extended polymer packing and providing a structural foundation for fibrillar network formation.

The impact of this crystallization behavior on the morphology was directly visualized by atomic force microscopy-infrared spectroscopy (AFM-IR) mapping at 1308 cm^{-1}, corresponding to the characteristic vibration of P(NDI2OD-T2) (Fig. S5 in ESI). As shown in Fig. 2(e), the CB-processed films display coarse, irregular aggregates, whereas *o*-DCB processing yields a well-developed, interconnected fibrillar network with a characteristic fibril width of about 50 nm (Fig. S6 in ESI). The

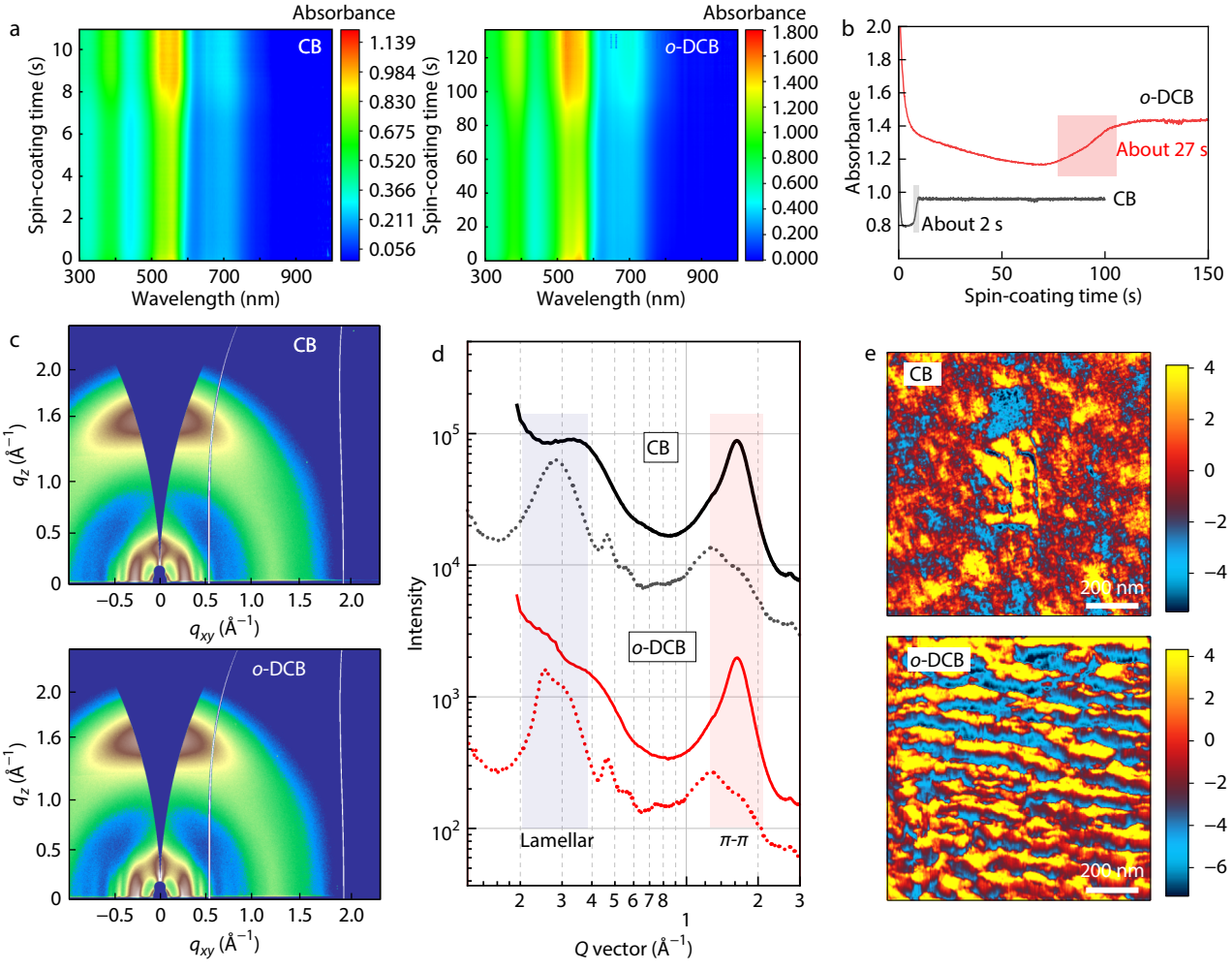

Fig. 2 (a) 2D contour images of *in situ* UV-Vis-NIR spectra of PQM-Cl:P(NDI2OD-T2) blend films processed from CB and *o*-DCB; (b) The absorbance of PQM-Cl (λ about 560 nm) as a function of spin-coating time; (c) GIWAXS scattering patterns and (d) corresponding sector-averaged *I*-*q* profiles of PQM-Cl:P(NDI2OD-T2) blend films processed from CB and *o*-DCB; (e) AFM-IR images of the blend films acquired at 1308 cm^{-1}. The color scale represents the IR amplitude, and the scale bar is 200 nm.

https://doi.org/10.1007/s10118-026-3746-y

elevated IR amplitude within the fibrils indicates a higher domain purity, which is consistent with crystallization-induced phase separation. Resonant soft X-ray scattering (RSoXS) was used to probe the morphology (Fig. S7 in ESI). No pronounced scattering peak was observed in the *I*-*q* curves, which can be attributed to the limited resonant contrast between the donor and acceptor components with similar conjugated backbones. Instead, the *o*-DCB-processed film exhibited a pronounced low-*q* intensity upturn, which corresponds to enhanced scattering from larger length-scale structures ($d = 2\pi/q$) and suggests the formation of larger and more phase-pure domains. To further verify the role of molecular weight in fibrillar-network formation, a low-molecular-weight batch of PQM-Cl was used as a control. This PQM-Cl batch exhibited markedly enhanced solubility in CB, as shown by solubility analysis (Fig. S8 in ESI). When blended with P(NDI2OD-T2) under the same processing conditions, low-molecular-weight PQM-Cl failed to develop an interconnected fibrillar network and instead formed coarse aggregates (Fig. S9 in ESI), highlighting the critical role of high molecular weight PQM-Cl in fibrillar network formation. These results demonstrate that enhanced crystallization in high-molecular-weight blends drives the formation of high-purity interconnected polymer fibrils, establishing a mechanically percolated and electronically continuous network that underpins both effective strain accommodation and charge transport preservation under deformation.

Mechanical Properties

The phase-separated morphology was strongly correlated with the mechanical response of the blend films. Representative tensile stress-strain (σ-ε) curves are shown in Fig. 3(a). The *o*-DCB-processed blend exhibited a fracture strain of 80.55% and a markedly higher toughness than the CB-processed blend, which fractured at 51.47%. Notably, the yield strain of the *o*-DCB blend reached 9.56%, representing a 1.6-fold increase over that of the CB blend, indicating enhanced structural integrity and delayed plastic deformation under the applied strain. Additional σ-ε measurements show the same trend of enhanced mechanical properties in the *o*-DCB-processed thin films. These results also confirmed the statistical reliability and reproducibility of the mechanical data (Fig. S10 in ESI). In comparison, neat high-molecular-weight PQM-Cl and P(NDI2OD-T2) films exhibited substantially lower fracture strains than the corresponding blend films (Fig. S11 in ESI), indicating that the high molecular weight of a single isolated component was insufficient to account for its exceptional mechanical properties. These results suggest that the enhanced mechanical robustness arises from the interpenetrating fibrillar network formed in the high-molecular-weight donor:acceptor blend.

Cyclic tensile tests were conducted to further investigate the strain-energy dissipation capability (Fig. 3b). Under an identical applied strain of 20%, the *o*-DCB-processed film exhibited a significantly larger hysteresis area between the loading and unloading curves than the CB-processed film, corresponding to energy dissipation values of 6.61 and 5.24 MJ·m^{-3}, respectively (Figs. 3b and 3c). The damping capacity, defined as the ratio of dissipated energy to total input energy, reached 82.3% for the *o*-DCB blend, exceeding the 75.5% observed for the CB blend. These results indicate that the high-

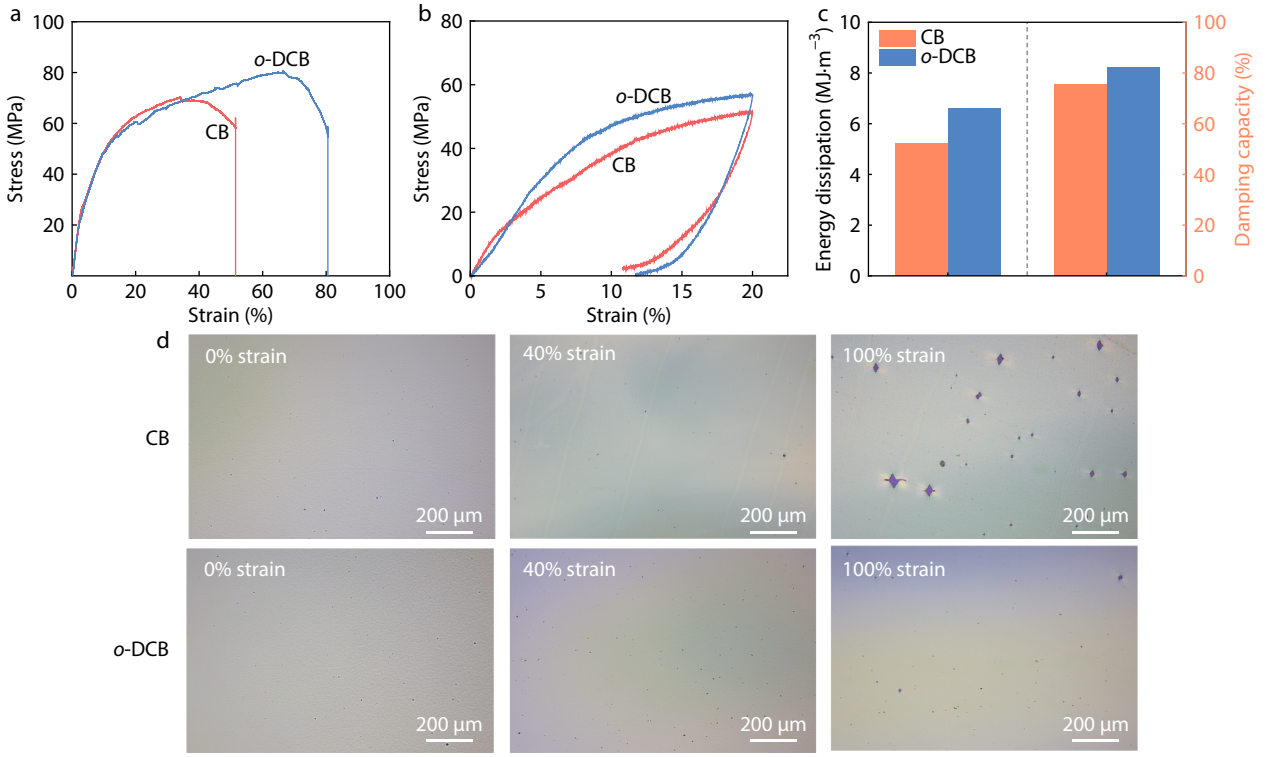

Fig. 3 (a) Stress-strain curves and (b) cyclic tensile loading-unloading curves of PQM-Cl:P(NDI2OD-T2) blend films processed from CB and *o*-DCB; (c) Comparison of energy dissipation and damping capacity for the blend films; (d) Optical microscopy images of blend films transferred onto PDMS substrates under different applied tensile strains.

https://doi.org/10.1007/s10118-026-3746-y

molecular-weight fibrillar network provides efficient pathways for strain-energy dissipation during large deformations.

To evaluate the mechanical performance of the supporting elastomer substrate, thin films were transferred onto polydimethylsiloxane (PDMS) membranes, and crack-onset strain (COS) was monitored by optical microscopy (Fig. 3d). The CB-processed film developed extensive irreversible microcracks at 40% strain, whereas the *o*-DCB-processed film maintained its structural integrity even at 100% strain without observable cracking. This striking contrast confirms that the interconnected fibrillar network effectively translates the molecular packing and mesoscale morphology into macroscopic film cohesion, thereby suppressing crack initiation and propagation under extreme deformation.

Photodetection Performance

To evaluate the photodetection performance independent of mechanical deformation, rigid OPDs were fabricated with conventional ITO/PEDOT:PSS/active layer/PNDIT-F3N-Br/Ag, where the active layer was PQM-Cl:P(NDI2OD-T2) blend film processed from CB or *o*-DCB, and the thickness was optimized to about 300 nm for both conditions (Fig. S12 in ESI). Fig. 4(a) shows the representative dark current density-voltage (J_d-V) characteristics. Compared with the CB-processed device, the *o*-DCB device exhibits a consistently reduced dark current under reverse bias, reaching 2.42×10^{-8} A·cm^{-2} at −0.1 V. Correspondingly, the external quantum efficiency (EQE) spectra measured at −0.1 V reveal enhanced photon-to-current conversion for the *o*-DCB device across the 400–700 nm spectral range (Fig. 4b). The concurrent suppression of dark current and enhancement of EQE translate into a markedly improved specific detectivity (D^*), which reaches 2.18×10^{12} Jones at 570 nm for the *o*-DCB device, compared with 1.65×10^{12} Jones for the CB counterpart (Fig. 4c). The noise power spectral density (S_n) of the *o*-DCB device was consistently lower in the low-frequency regime (Fig. S13 in ESI), which is indicative of reduced flicker noise and suppressed carrier-trapping dynamics.

To elucidate the physical origin of the enhanced photodetection performance, we first examined the internal electric field characteristics of the devices. Capacitance-voltage (*C*-*V*) measurements revealed a higher built-in potential (V_{bi}) for the *o*-DCB device (0.789 V) than for the CB device (0.733 V) (Fig. S14 in ESI), suggesting a more efficient charge separation.[41] Furthermore, capacitance-frequency (*C*-*F*) analysis allows the extraction of the trap density of states (tDOS) as a function of energy. As shown in Fig. 4(d), the *o*-DCB device exhibited a moderately reduced tDOS (at about 0.49 eV, implying partial suppression of deep-trap states. These results indicate that the morphology formed under *o*-DCB processing improves donor-acceptor percolation while mitigating electronic disorder, both of which are essential for lowering the dark current.[42]

Charge transport and recombination were further investigated to establish a direct link between the morphology and carrier dynamics. Space-charge-limited current (SCLC) measurements performed on hole-only and electron-only devices revealed enhanced hole (μ_h) and electron (μ_e) mobilities in the *o*-DCB-processed blend films (Fig. S15 and Table S3 in ESI), reflecting the improved transport within the bulk active layer. Complementarily, photo-CELIV measurements probe carrier extraction dynamics under operational device conditions and show a higher effective carrier mobility for *o*-DCB-processed OPDs (Fig. 4e). The consistent mobility enhancement observed in both bulk- and device-level measurements suggests the formation of a well-connected transport network. Charge recombination was probed by light-intensity-dependent measurements of the short-circuit current and

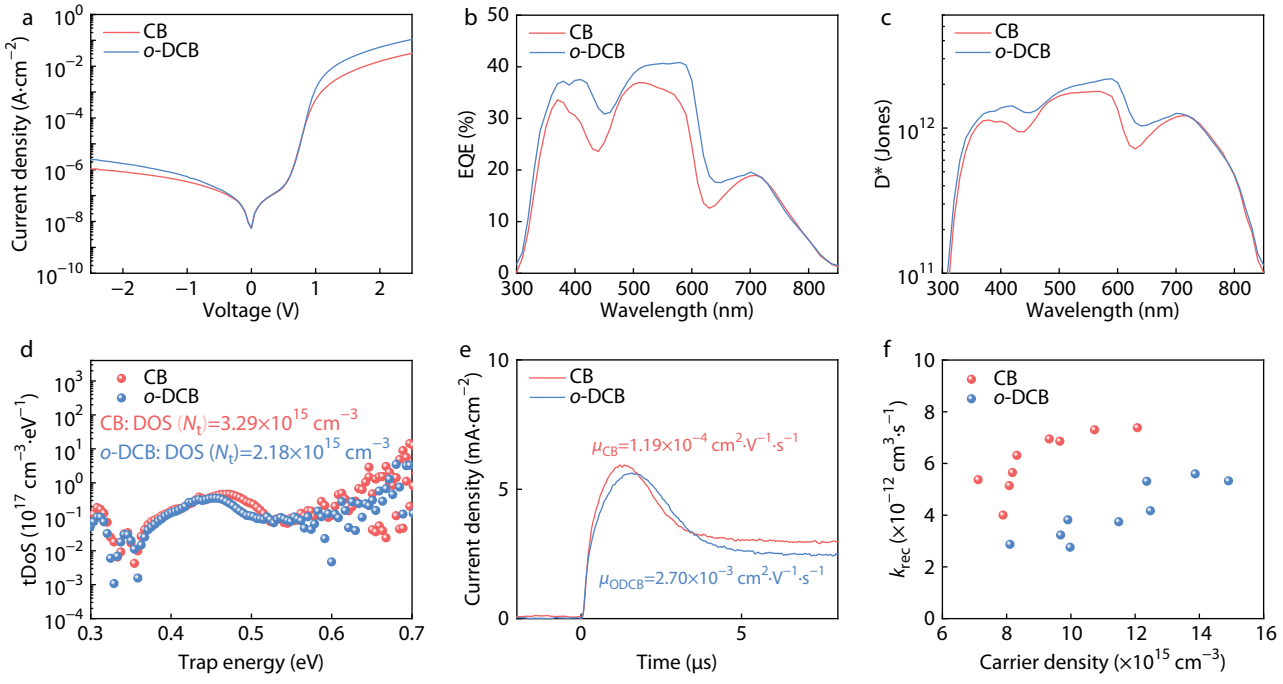

Fig. 4 (a) Dark *J*-*V* characteristics, (b) EQE spectra at −0.1 V, (c) D^* derived from EQE and J_d at −0.1 V, (d) tDOS as a function of energy, (e) photo-CELIV transients, and (f) carrier recombination rate of PQM-Cl:P(NDI2OD-T2) based OPDs processed from CB and *o*-DCB.

https://doi.org/10.1007/s10118-026-3746-y

open-circuit voltage, which indicated reduced trap-assisted recombination in the *o*-DCB devices (Fig. S16 in ESI). Transient photovoltage measurements further revealed a lower recombination rate constant (k_{rec}),[43] corroborating the more efficient charge extraction (Fig. 4f).

These results demonstrate that the kinetically controlled fibrillar network morphology formed from high-molecular-weight conjugated polymer blends simultaneously promotes efficient charge transport and suppresses trap-mediated recombination. This morphology-enabled balance between low electronic disorder and robust percolation pathways underpins the reduced J_d and enhanced D^* observed in *o*-DCB-processed OPDs.

Given the balance between mechanical and photodetection performance, IS-OPDs were fabricated with a TPU/PEDOT:PSS (M-PH1000)/PEDOT:PSS (4083)/active layer/PNDIT-F3N-Br/EGaIn@Ag structure, where M-PH1000 and EGaIn@Ag served as stretchable transparent and back electrodes, respectively (Fig. 1a).[28] No additional external encapsulation layer was applied in this work; the EGaIn@Ag back electrode formed a native gallium oxide skin in air, which helped stabilize the liquid metal electrode and suppress leakage during mechanical deformation. The devices processed from CB and *o*-DCB were systematically compared.

Representative dark *J*-*V* characteristics under tensile strain are shown in Figs. 5(a) and 5(b), and the evolution of J_d at −0.1 V is summarized in Fig. 5(c). For CB-processed devices, the reverse-bias J_d increases sharply beyond 30% strain, rising from 1.95×10^{-7} A·cm^{-2} at 0% strain to 2.07×10^{-6} A·cm^{-2} at 30% strain and further to 1.18×10^{-4} A·cm^{-2} at 70% strain, accompanied by a collapse of the rectification ratio to near unity. This behavior indicated the formation of irreversible leakage pathways and electrical failure under deformation. In contrast, *o*-DCB-processed devices maintained a stable J_d of the order of 10^{-8} A·cm^{-2} with minimal variation up to 40% strain, demonstrating markedly enhanced electrical robustness. At higher strains (60% and 70%), a non-monotonic variation in J_d is observed, which is likely associated with the degradation of the rectification behavior under large deformation. Additional strain-dependent dark *J*-*V* curves showed similar trends (Fig. S17 and Table S4 in ESI). These variations may originate from the formation of localized microcracks and interfacial inhomogeneities, which introduce additional leakage pathways and reduce the effectiveness of the injection barrier. The environmental stability of IS-OPDs was also evaluated in air. As shown in Fig. S18 (in ESI), *o*-DCB-processed devices retain more stable strain-dependent dark *J*-*V* characteristics compared to the CB-processed devices after air exposure, which can be attributed to the mechanically robust fibrillar network morphology.

Consistent with the dark current evolution, the EQE spectra of both devices gradually decreased with increasing strain (Figs. 5d and 5e), suggesting a reduced carrier collection efficiency and enhanced trap-assisted recombination induced by mechanical deformation.[44] The resulting strain-dependent D^* values are shown in Fig. 5(f). The *o*-DCB-processed devices exhibit negligible degradation in D^*, maintaining values around 1.89×10^{12} Jones up to 40% strain, whereas CB-processed devices suffer pronounced performance loss at 30% strain. The key performance metrics are summarized in Table 1. Therefore, these results demonstrate that the interconnected fibrillar network formed by high-molecular-weight conjugated polymers effectively translates microscopic structural integrity into macroscopic device stability, enabling IS-OPDs with robust mechanical resilience and reliable photodetection performance under large deformations.

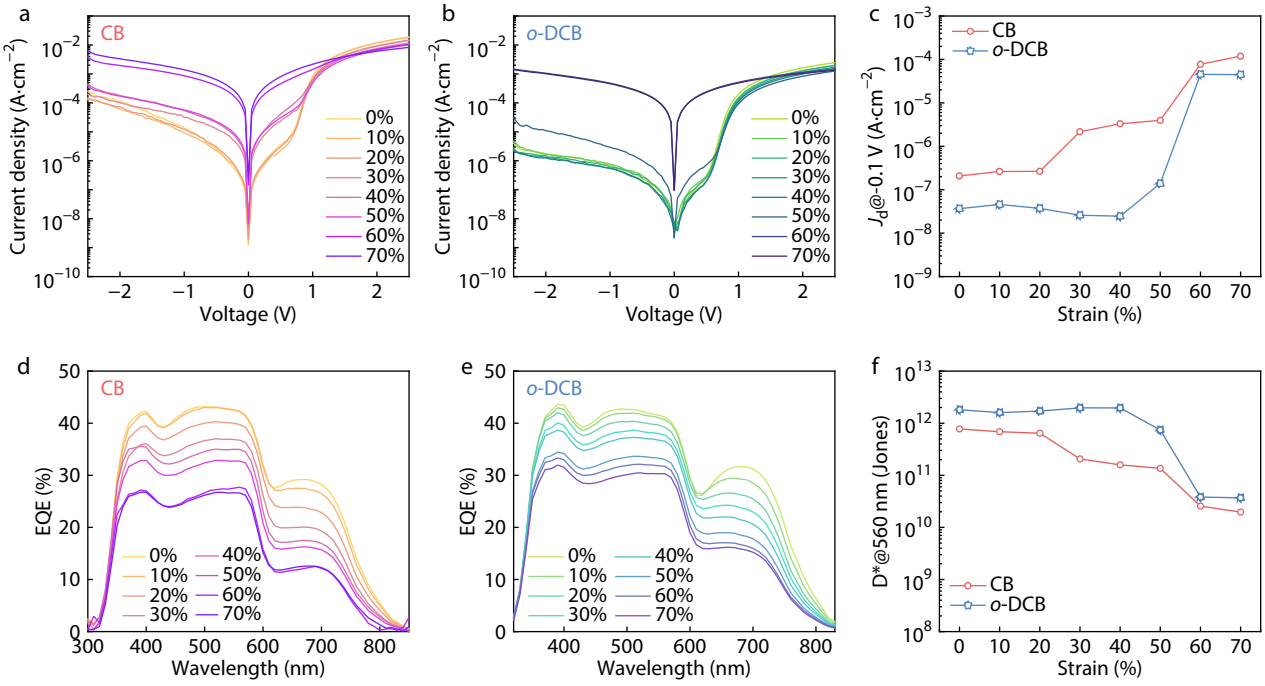

Fig. 5 Strain-dependent dark *J*-*V* characteristics of IS-OPDs processed by (a) CB and (b) *o*-DCB; (c) Dark current density at −0.1 V as a function of strain. Strain-dependent EQE spectra of IS-OPDs processed by (d) CB and (e) *o*-DCB; (f) D^* at 560 nm under −0.1 V as a function of strain.

Practical Applications of Stretchable Device

Stable and mechanically robust IS-OPDs are essential for emerging applications such as deformable optical communication systems and wearable imaging platforms. As proof-of-concept

Table 1 Summary of performance metrics for IS-OPDs under different strains.

Device	Strain (%)	J_d@–0.1 V (A·cm^{-2})	EQE@560 nm (%)	R (A·W^{-1})	D^*@560 nm (Jones)
CB	0%	1.95×10^{-7}	42.20	0.191	7.64×10^{11}
	10%	2.48×10^{-7}	42.32	0.191	6.78×10^{11}
	20%	2.50×10^{-7}	39.74	0.179	6.33×10^{11}
	30%	2.07×10^{-6}	36.75	0.166	2.04×10^{11}
	40%	3.17×10^{-6}	34.96	0.158	1.57×10^{11}
	50%	3.79×10^{-6}	32.75	0.148	1.34×10^{11}
	60%	7.57×10^{-5}	27.72	0.125	2.54×10^{10}
	70%	1.18×10^{-4}	26.62	0.120	1.95×10^{10}
o-DCB	0%	3.40×10^{-8}	41.19	0.186	1.78×10^{12}
	10%	4.25×10^{-8}	40.68	0.184	1.58×10^{12}
	20%	3.45×10^{-8}	39.24	0.177	1.68×10^{12}
	30%	2.39×10^{-8}	37.71	0.170	1.94×10^{12}
	40%	2.27×10^{-8}	36.55	0.165	1.93×10^{12}
	50%	1.30×10^{-7}	33.04	0.149	7.32×10^{11}
	60%	4.44×10^{-5}	31.72	0.143	3.79×10^{10}
	70%	4.36×10^{-5}	30.32	0.137	3.67×10^{10}

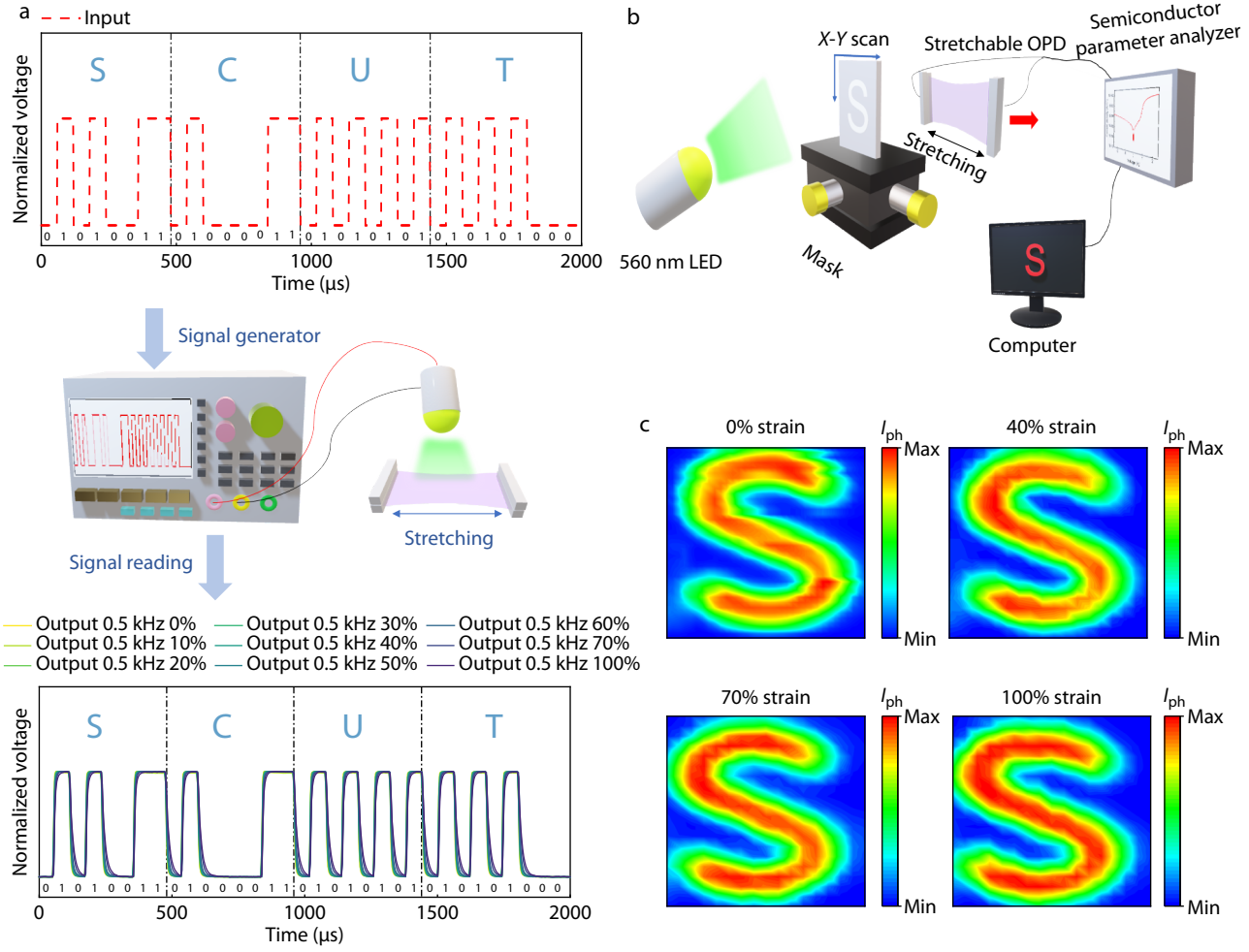

Fig. 6 (a) Schematic illustration of the optical communication system based on IS-OPDs and the corresponding output pulse signals recorded under 560 nm optical pulses modulated at 0.5 kHz with a bias of –0.1 V; (b) Schematic of the single-pixel imaging setup using an IS-OPD, where a stainless-steel mask patterned with the letter "S" is employed for spatial modulation and the photocurrent is collected at 0 V bias; (c) Reconstructed single-pixel images of the "S" pattern obtained at tensile strains of 0%, 40%, 70%, and 100%.

demonstrations, we showcase optical communication and strain-resilient single-pixel imaging enabled by *o*-DCB-processed IS-OPDs.

The transient photoresponse of the IS-OPD was evaluated under pulsed 560 nm illumination. The device exhibited fast rise and decay dynamics with a high signal-to-noise ratio, indicative of efficient charge extraction and minimal carrier trapping. The rise and fall time were on the microsecond scale (Fig. S19 and Table S5 in ESI), corresponding to an operational bandwidth in the kilohertz (kHz) range, which is well matched to the modulation frequencies (0.5−5.0 kHz) used in the optical communication demonstration. The transient responses measured over a range of modulation frequencies further confirmed the capability of the device for high-speed optical signal detection (Fig. S20 in ESI), which supports its use in optical communication. In addition, the IS-OPDs exhibited a wide and strain-insensitive linear dynamic range (LDR), maintaining values above 105 dB up to 40% strain (Fig. S21 in ESI), which ensures a broad linear operating window for light detection and thereby preserves signal fidelity during optical signal transmission. Fig. 6(a) shows the output pulse signals recorded at a modulation frequency of 0.5 kHz with a bias of −0.1 V. Notably, the transient photoresponse remains stable under large applied tensile strains. To demonstrate strain-tolerant optical communication, a simple word, "SCUT," was encoded using the American Standard Code for Information Interchange (ASCII) format, in which optical signals corresponding to binary "0" and "1" were clearly distinguished and accurately reproduced by the IS-OPD even at 100% strain.

The IS-OPD was implemented in a single-pixel imaging system. As illustrated in Fig. 6(b), an "S"-shaped mask was placed above the device mounted on a programmable *x*-*y* translation stage, and the spatially resolved photocurrent was reconstructed under increasing tensile strain. As shown in Fig. 6(c), the device preserved a clear imaging contrast and spatial fidelity at strains of 0%, 40%, 70%, and 100%.

These application demonstrations provide direct evidence that the interconnected fibrillar morphology induced by high-molecular-weight conjugated polymer blends enables the simultaneous achievement of superior mechanical robustness and reliable optoelectronic functionality, thereby supporting the use of IS-OPDs in advanced deformable optoelectronic systems. From the perspective of practical applications, stretchable optoelectronic devices are required to accommodate the strain levels encountered in typical human motions such as finger joints (about 42%), wrist bending (about 45%), elbow movement (about 63%), and knee flexion (about 100%).[45] In this context, our high-molecular-weight polymer-based IS-OPDs maintained stable optoelectronic performance up to 70% strain and remained operational even at 100% strain, demonstrating mechanical robustness that meets or exceeds the requirements of most wearable and bio-integrated applications.

CONCLUSIONS

We demonstrate that crystallization-driven fibrillar networks formed by high-molecular-weight conjugated polymers provide an effective route for resolving the long-standing trade-off between mechanical stretchability and optoelectronic performance in intrinsically stretchable organic photodetectors. The interconnected fibrils composed of entangled polymer chains enable efficient dissipation of strain energy through network-level deformation rather than *via* localized crystallite fracture or reorientation, resulting in high fracture strain and enhanced toughness. Meanwhile, the high-purity conjugated network on the tens-of-nanometers length scale establishes continuous charge-transport pathways, leading to improved carrier mobility and suppressed recombination.

The presented IS-OPDs based on the PQM-Cl:P(NDI2OD-T2) blend exhibited stable photodetection performance with a specific detectivity of 1.89×10^{12} Jones maintained up to 40% tensile strain and supported reliable optical communication with high signal-to-noise ratios as well as single-pixel imaging even under 100% strain. These results establish high-molecular-weight conjugated polymer fibrillar networks as key structural motifs for IS-OPDs, enabling large-strain stretchability without compromising performance reliability. More broadly, our study highlights the critical role of molecular weight and processing control in governing both the mechanical and optoelectronic properties. For next-generation polymeric acceptors, optimizing the molecular weight in conjunction with controlled pre-aggregation and film formation kinetics is essential for simultaneously achieving a broad spectral response range, high detectivity, and mechanical stability.

Conflict of Interests

The authors declare no interest conflict.

Electronic Supplementary Information

Electronic supplementary information (ESI) is available free of charge in the online version of this article at http://doi.org/10.1007/s10118-026-3746-y.

Data Availability Statement

The data that support the findings of this study are available from the corresponding author upon reasonable request.

ACKNOWLEDGMENTS

This work was financially supported by the National Key R&D Program of China (No. 2023YFB3609000), the National Natural Science Foundation of China (No. U25A20262), State Key Laboratory of Luminescent Materials and Devices, South China University of Technology (No. Skllmd-2025-09), and the Anhui Provincial Natural Science Foundation (No. 2308085MA19). RSoXS was performed at the Jinhua beamline BL05U-B of the Hefei Light Source. GIWAXS was performed at beamline 7.3.3 at the Advanced Light Source, a U.S. DOE Office of Science User Facility under contract no. DE-AC02-05CH11231.

Graphical Abstract

Robust Intrinsically Stretchable Organic Photodetectors Enabled by High-molecular-weight Conjugated Polymer Fibrils

He-Bing Nie, Lu Hao, Jing-Chuan Chen, Zhi-Yuan Yang, Xue-Fei Wu, Zhi-Qin Xia, Wan-Cheng Yu, Xue-Chen Jiao, Wen-Kai Zhong, and Fei Huang

South China University of Technology, China; Institute of Chemistry, Chinese Academy of Sciences, China; Lawrence Berkeley National Laboratory, United States; University of Science and Technology of China, China

High-molecular-weight conjugated polymer blends form entangled fibrillar networks in intrinsically stretchable organic photodetectors. The mechanically percolated fibrils dissipate strain and suppress cracking while maintaining continuous charge transport, thus enabling high toughness, about 80% fracture strain, and stable detectivity (about 10^{12} Jones) under large deformations for optical communication and imaging.

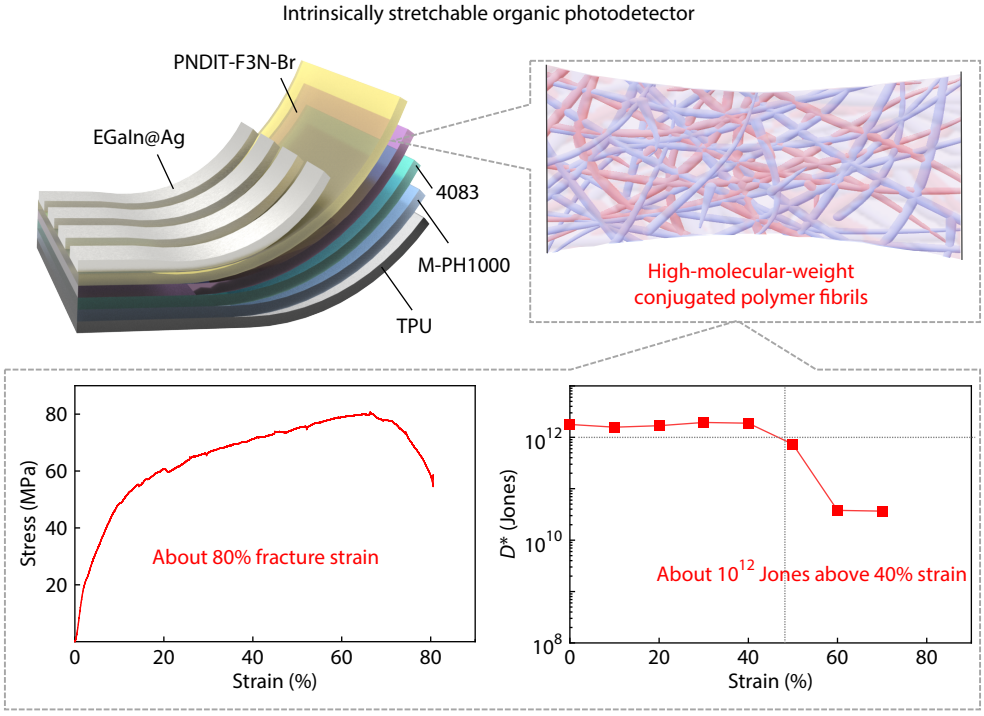

Chinese J. Polym. Sci. 2026 *https://doi.org/10.1007/s10118-026-3746-y*

REFERENCES

1 Chang, S.; Koo, J. H.; Yoo, J.; Kim, M. S.; Choi, M. K.; Kim, D. H.; Song, Y. M. Flexible and stretchable light-emitting diodes and photodetectors for human-centric optoelectronics. *Chem. Rev.* **2024**, *124*, 768–859.

2 Bai, X.; Gao, W.; Cai, Y.; Bai, Z.; Qi, Y.; Yan, B.; Wang, Y.; Lu, Z.; Ding, J. Advanced stretchable photodetectors: strategies, materials and devices. *Chem. Eur. J.* **2023**, *29*, e202203022.

3 Araki, T.; Li, K.; Suzuki, D.; Abe, T.; Kawabata, R.; Uemura, T.; Izumi, S.; Tsuruta, S.; Terasaki, N.; Kawano, Y.; Sekitani, T. Broadband photodetectors and imagers in stretchable electronics packaging. *Adv. Mater.* **2024**, *36*, 2304048.

4 Lee, Y.; Oh, J. Y.; Xu, W.; Kim, O.; Kim, T R.; Kang, J.; Kim, Y.; Son, D.; Tok, J B. H.; Park, M. J.; Bao, Z.; Lee, T. W. Stretchable organic optoelectronic sensorimotor synapse. *Sci. Adv.* **2018**, *4*, eaat7387.

5 Gu, L.; Poddar, S.; Lin, Y.; Long, Z.; Zhang, D.; Zhang, Q.; Shu, L.; Qiu, X.; Kam, M.; Javey, A. A biomimetic eye with a hemispherical perovskite nanowire array retina. *Nature* **2020**, *581*, 278–282.

6 Park, J. S.; Kim, G. U.; Lee, S.; Lee, J. W.; Li, S.; Lee, J. Y.; Kim, B. J. Material design and device fabrication strategies for stretchable organic solar cells. *Adv. Mater.* **2022**, *34*, 2201623.

7 Jeon, H.; Oh, J.; Lee, J. W.; Eun, H. J.; Kang, W. J.; Ryu, D. H.; Song, C. E.; Wang, C.; Kang, H.; Kim, T. S.; Kim, J. H.; Lee, S.; Kim, B. J. Strain-induced detectivity enhancement in intrinsically stretchable organic photodetectors. *Adv. Mater.* **2026**, *38*, e14951.

8 Chow, P. C. Y.; Someya, T. Organic photodetectors for next-generation wearable electronics. *Adv. Mater.* **2020**, *32*, 1902045.

9 Wang, Z.; Zhang, D.; Yang, L.; Allam, O.; Gao, Y.; Su, Y.; Xu, M.; Mo, S.; Wu, Q.; Wang, Z.; Liu, J.; He, J.; Li, R.; Jia, X.; Li, Z.; Yang, L.; Weber, M. D.; Yu, Y.; Zhang, X.; Marks, T. J.; Stingelin, N.; Kacher, J.; Jang, S. S.; Facchetti, A.; Shao, M. Mechanically robust and stretchable organic solar cells plasticized by small-molecule acceptors. *Science* **2025**, *387*, 381–387.

10 Shi, W.; Guo, Y.; Liu, Y. When flexible organic field-effect transistors meet biomimetics: a prospective view of the internet of things. *Adv. Mater.* **2020**, *32*, 1901493.

11 Zhang, Z.; Wang, W.; Jiang, Y.; Wang, Y. X.; Wu, Y.; Lai, J. C.; Niu, S.; Xu, C.; Shih, C. C.; Wang, C.; Yan, H.; Galuska, L.; Prine, N.; Wu, H. C.; Zhong, D.; Chen, G.; Matsuhisa, N.; Zheng, Y.; Yu, Z.; Wang, Y.; Dauskardt, R.; Gu, X.; Tok, J. B. H.; Bao, Z. High-brightness all-polymer stretchable LED with charge-trapping dilution. *Nature* **2022**, *603*, 624–630.

12 Wang, S.; Zhong, W.; Huang, F. Recent advancements in Stretchable Polymer Optoelectronics. *Acta Polymerica Sinica* (in Chinese) **2024**, *55*, 1091–1110.

13 Qin, M.; Bian, Y.; Wang, C.; Sun, J.; Shi, W.; Liu, K.; Zheng, Y.; Zhang, F.; Liu, G.; Shao, M.; Wen, W.; Zhu, Z.; Zhu, M.; Zhao, Z.; Wang, H.; Liu, Y.; Yuan, G.; Guo, Y. Intrinsically stretchable organic photodiodes for faint near-infrared light detection and extendable cryptographic imaging. *Adv. Funct. Mater.* **2024**, *34*, 2403770.

14 Peng, Z.; Chen, R.; Liu, X.; Zhang, Y.; Wang, J.; Miao, J.; Han, Y.; Liu, J. Nanoconfinement effect enhances stretchability and mechanical stability of organic photodetectors. *Adv. Funct. Mater.* **2025**, *35*, 2410390.

15 Wang, Y.; Li, M.; Wang, R.; Shi, H.; Li, F.; Zhu, Y.; Li, G.; Ni, W.; Chen, Y.; Li, M.; Geng, Y. Highly stretchable transparent electrodes for wearable near-infrared organic photodetectors enabling vital monitoring, imaging, and communication. *ACS Appl. Mater. Interfaces* **2025**, *17*, 42162–42173.

16 Wang, J.; Wang, Y.; Xian, K.; Qiao, J.; Chen, Z.; Bi, P.; Zhang, T.; Zheng, Z.; Hao, X.; Ye, L.; Zhang, S.; Hou, J. Regulating phase separation kinetics for high-efficiency and mechanically robust all-polymer solar cells. *Adv. Mater.* **2024**, *36*, 2305424.

17 He, H.; Li, X.; Zhang, J.; Chen, Z.; Gong, Y.; Zhuo, H.; Wu, X.; Li, Y.; Wang, S.; Bi, Z.; Song, B.; Zhou, K.; Liang, T.; Ma, W.; Lu, G.; Ye, L.; Meng, L.; Zhang, B.; Li, Y.; Li, Y. Dynamic hydrogen-bonding enables high-performance and mechanically robust organic solar cells processed with non-halogenated solvent. *Nat. Commun.* **2025**, *16*, 787

18 Wan, Q.; Seo, S.; Lee, S. W.; Lee, J.; Jeon, H.; Kim, T. S.; Kim, B. J.; Thompson, B C. High-performance intrinsically stretchable polymer solar cell with record efficiency and stretchability enabled by thymine-functionalized terpolymer. *J. Am. Chem. Soc.* **2023**, *145*, 11914–11920.

19 Liu, D.; Lei, Y.; Ji, X.; Wu, Y.; Lin, Y.; Wang, Y.; Zhang, S.; Zheng, Y.; Chen, Y.; Lai, J. C.; Zhong, D.; Cheng, H. W.; Chiong, J A.; Gu, X.; Gam, S.; Yun, Y.; Tok, J. B H.; Bao, Z. Tuning the mechanical and electric properties of conjugated polymer semiconductors: side-chain design based on asymmetric benzodithiophene building blocks. *Adv. Funct. Mater.* **2022**, *32*, 2203527.

20 Huang, Y. W.; Lin, Y. C.; Yen, H. C.; Chen, C. K.; Lee, W. Y.; Chen, W. C.; Chueh, C. C. High mobility preservation of near amorphous conjugated polymers in the stretched states enabled by biaxially-extended conjugated side-chain design. *Chem. Mater.* **2020**, *32*, 7370–7382.

21 Luo, X.; Liu, X.; Lin, Y.; Li, M.; Yang, Z.; Xiong, Z.; Wang, Y.; Peng, F.; Zhong, W.; Li, N.; Ying, L. Modular design of polymer donors regulates solution aggregation and stretchability of organic solar cells. *Angew. Chem. Int. Ed.* **2025**, *64*, e202514985.

22 Zhu, M.; Shao, Z.; Li, Y.; Xiong, Z.; Yang, Z.; Chen, J.; Shi, W.; Wang, C.; Bian, Y.; Zhao, Z.; Guo, Y.; Liu, Y. Molecular-scale geometric design: zigzag-structured intrinsically stretchable polymer semiconductors. *J. Am. Chem. Soc.* **2024**, *146*, 27429–27442.

23 Guan, C.; Xiao, C.; Liu, X.; Hu, Z.; Wang, R.; Wang, C.; Xie, C.; Cai, Z.; Li, W. Non-covalent interactions between polyvinyl chloride and conjugated polymers enable excellent mechanical properties and high stability in organic solar cells. *Angew. Chem. Int. Ed.* **2023**, *62*, e202312357.

24 Wang, Y.; Chen, K. L.; Awada, A.; Prine, N.; Cao, Z.; Zhu, C.; Chiu, Y. C.; Rondeau-Gagné, S.; Gu, X. Leveraging non-covalent interactions to control the morphology and electrical and mechanical properties of stretchable semiconducting composites. *Chem. Mater.* **2023**, *35*, 9713–9724.

25 Luo, X.; Freychet, G.; Gan, Z.; An, K.; Du, H.; Wang, C.; Li, N.; Zhong, W.; Ying, L. Intrinsically stretchable organic photovoltaic thin films enabled by optimized donor–acceptor pairing. *Macromolecules* **2023**, *56*, 8928–8938.

26 Mullin, W. J.; Sharber, S. A.; Thomas Iii, S. W. Optimizing the self-assembly of conjugated polymers and small molecules through structurally programmed non-covalent control. *J. Polym Sci.* **2021**, *59*, 1643–1663.

27 Zheng, Y.; Yu, Z.; Zhang, S.; Kong, X.; Michaels, W.; Wang, W.; Chen, G.; Liu, D.; Lai, J. C.; Prine, N.; Zhang, W.; Nikzad, S.; Cooper, C. B.; Zhong, D.; Mun, J.; Zhang, Z.; Kang, J.; Tok, J. B. H.; McCulloch, I.; Qin, J.; Gu, X.; Bao, Z. A molecular design approach towards elastic and multifunctional polymer electronics. *Nat. Commun.* **2021**, *12*, 5701.

28 Li, S.; Gao, M.; Zhou, K.; Li, X.; Xian, K.; Zhao, W.; Chen, Y.; He, C.; Ye, L. Achieving record-high stretchability and mechanical stability in organic photovoltaic blends with a dilute-absorber strategy. *Adv. Mater.* **2024**, *36*, 2307278.

29 Zuo, J.; Han, D.; Yao, H.; Kuvondikov, V.; Ye, L. Stretching the future: strategies and emerging trends in stretchable organic photovoltaic materials. *Energy Environ. Sci.* **2025**, *18*, 6344–6365.

30 Yang, W.; Luo, X.; Li, M.; Shi, C.; Wang, Z.; Yang, Z.; Wu, J.; Zhang, X.; Huang, W.; Ma, D.; Wang, C.; Zhong, W.; Ying, L. Achieving efficient intrinsically stretchable organic photovoltaics with a conjugated and elastomeric dual-network morphology. *Adv. Energy Mater.* **2025**, *15*, 2403259.

31 Zuo, J.; Jin, T.; Li, H.; Li, J.; Liu, X.; Yu, X.; Han, Y.; Han, Y. Continuous conjugated polymer network in elastomer matrix arising from solution-state aggregation and film-forming dynamics favoring mechanical and electrical properties. *Adv. Funct. Mater.* **2025**, *35*, 2424785.

32 Ding, Z.; Liu, D.; Zhao, K.; Han, Y. Optimizing morphology to trade off charge transport and mechanical properties of stretchable conjugated polymer films. *Macromolecules* **2021**, *54*, 3907–3926.

33 Ding, Z.; Zhao, K.; Han, Y. Strain-induced morphology evolution and charge transport in conjugated polymer films. *Interdisciplinary Materials* **2025**, *4*, 138–161.

34 Rivnay, J.; Mannsfeld, S. C. B.; Miller, C E.; Salleo, A.; Toney, M. F. Quantitative determination of organic semiconductor microstructure from the molecular to device scale. *Chem. Rev.* **2012**, *112*, 5488–5519.

35 Zhu, L.; Zhang, M.; Xu, J.; Li, C.; Yan, J.; Zhou, G.; Zhong, W.; Hao, T.; Song, J.; Xue, X.; Zhou, Z.; Zeng, R.; Zhu, H.; Chen, C. C.; MacKenzie, R. C. I.; Zou, Y.; Nelson, J.; Zhang, Y.; Sun, Y.; Liu, F. Single-junction organic solar cells with over 19% efficiency enabled by a refined double-fibril network morphology. *Nat. Mater.* **2022**, *21*, 656–663.

36 Zhu, L.; Zhang, M.; Zhou, Z.; Zhong, W.; Hao, T.; Xu, S.; Zeng, R.; Zhuang, J.; Xue, X.; Jing, H.; Zhang, Y.; Liu, F. Progress of organic photovoltaics towards 20% efficiency. *Nat. Rev. Electr. Eng.* **2024**, *1*, 581–596.

37 Zhong, W.; Wang, S.; Liu, F. Unlocking functional potentials: nanofibril networks in organic semiconductors. *Adv. Nanocomp.*

2025, *2*, 124–147.
38 Xia, T.; Cai, Y.; Fu, H.; Sun, Y. Optimal bulk-heterojunction morphology enabled by fibril network strategy for high-performance organic solar cells. *Sci. China Chem.* **2019**, *62*, 662–668.
39 Li, D.; Deng, N.; Fu, Y.; Guo, C.; Zhou, B.; Wang, L.; Zhou, J.; Liu, D.; Li, W.; Wang, K.; Sun, Y.; Wang, T. Fibrillization of non-fullerene acceptors enables 19% efficiency pseudo-bulk heterojunction organic solar cells. *Adv. Mater.* **2023**, *35*, 2208211.
40 Wei, Y.; Zhou, X.; Cai, Y.; Li, Y.; Wang, S.; Fu, Z.; Sun, R.; Yu, N.; Li, C.; Huang, K.; Bi, Z.; Zhang, X.; Zhou, Y.; Hao, X.; Min, J.; Tang, Z.; Ma, W.; Sun, Y.; Huang, H. High performance as-cast organic solar cells enabled by a refined double-fibril network morphology and improved dielectric constant of active layer. *Adv. Mater.* **2024**, *36*, 2403294.
41 Nolasco, J C.; Sánchez-Díaz, A.; Cabré, R.; Ferré-Borrull, J.; Marsal, L F.; Palomares, E.; Pallarès, J. Relation between the barrier interface and the built-in potential in pentacene/C60 solar cell. *Appl. Phys. Lett.* **2010**, *97*, 013305.
42 Kublitski, J.; Hofacker, A.; Boroujeni, B K.; Benduhn, J.; Nikolis, V C.; Kaiser, C.; Spoltore, D.; Kleemann, H.; Fischer, A.; Ellinger, F.; Vandewal, K.; Leo, K. Reverse dark current in organic photodetectors and the major role of traps as source of noise. *Nat. Commun.* **2021**, *12*, 551.
43 Hamilton, R.; Shuttle, C. G.; O'Regan, B.; Hammant, T. C.; Nelson, J.; Durrant, J. R. Recombination in annealed and nonannealed polythiophene/fullerene solar cells: transient photovoltage studies versus numerical modeling. *J. Phys. Chem. Lett.* **2010**, *1*, 1432–1436.
44 Yang, W.; Luo, X.; Liu, J.; Chen, J.; Wu, X.; Fink, Z.; Shi, C.; Zhong, W.; Wang, C.; Ying, L. Dynamic disulfide bond networks enable self-healable and mechanically resilient intrinsically stretchable organic solar cells. *Energy Environ. Sci.* **2025**, *18*, 6597–6607.
45 Qin, J.; Lan, L.; Chen, S.; Huang, F.; Shi, H.; Chen, W.; Xia, H.; Sun, K.; Yang, C. Recent progress in flexible and stretchable organic solar cells. *Adv. Funct. Mater.* **2020**, *30*, 2002529.

https://doi.org/10.1007/s10118-026-3746-y